EXPERIMENTAL TESTING OF DYNAMICALLY OPTIMIZED PHOTOELECTRON BEAMS[*]

J.B. ROSENZWEIG, A.M. COOK, M. DUNNING, R.J. ENGLAND

UCLA Dept. of Physics and Astronomy, 405 Hilgard Ave.,

Los Angeles, CA 90095, USA

P. MUSUMECI[†], M. BELLAVEGLIA[#], M. BOSCOLO[#], L. CATANI[#], A. CIANCHI[#],
G. DI PIRRO[#], M. FERRARIO[#], D. FILLIPETTO[#], G. GATTI[#], L. PALUMBO[#],
L. SERAFINI[£], C. VICARIO[#]

[#]*Istituto Nazionale di Fisica Nucleare, Laboratori Nazionale di Frascati,*

Frascati (RM) Italy,

[†]*Istituto Nazionale di Fisica Nucleare, Sezione Roma 1*
Roma (RM) Italy

[£]*Istituto Nazionale di Fisica Nucleare, Sezione Milano Via Celoria*
Milano (MI) Italy

Jet Propulsion Laboratory, California Institue of Technology, 4800 Oak Grove Drive

Pasadena, CA 91101, USA

We discuss the design of and initial results from an experiment in space-charge dominated beam dynamics which explores a new regime of high-brightness electron beam generation at the SPARC (located at INFN-LNF, Frascati) photoinjector. The scheme under study employs the natural tendency in intense electron beams to configure themselves to produce a uniform density, giving a nearly ideal beam from the viewpoint of space charge-induced emittance. The experiments are aimed at testing the marriage of this idea with a related concept, emittance compensation, We show that the existing infrastructure at SPARC is nearly ideal for the proposed tests, and that this new regime of operating photoinjector may be the preferred method of obtaining highest brightness beams with lower energy spread. We discuss the design of the experiment, including developing of a novel time-dependent, aerogel-based imaging system. This system has been installed at SPARC, and first evidence for nearly uniformly filled ellipsoidal charge distributions recorded.

1. Introduction

In order to obtain the highest brightness electron beams from photoinjectors, it is most common to rely on the *emittance compensation* process[1]. Optimization of this process demands that the transverse fields be as uniform, and linear (in radius r) as possible. The existing theoretical and experimental studies of emittance compensation have, to that end, assumed use of a uniform density electron beam, having a cylindrical shape. However, this shape produces space-charge fields near the beam head and tail that have pronounced nonlinear dependences on the spatial coordinates. These nonlinearities result in both transverse and longitudinal emittance growth.

It has been known for some time[2], however, that a uniform ellipsoidal density distribution yields space-charge fields that are linear in all dimensions (e.g. $E_x \propto x$, $E_z \propto z$). Under such conditions, it is conceivable that one may obtain essentially emittance growth-free dynamics. How to produce such a distribution has, until recently, remained an unanswered question.

In 1997, Serafini proposed the dynamic creation of an ellipsoidal bunch by launching an ultra-short, radially shaped beam[3], which then evolves through longitudinal expansion of differing radii in the beam to achieve the desired longitudinal shape. In this work, a 10's of femtosecond laser pulse with uniform time profile was assumed, which is not technically feasible — pulses this short are now a routine capability of the photocathode drive lasers, but not with such a restrictive profile. On the other had, it has recently been shown by Luiten, *et al.,*[4] that in obtaining the correct final ellipsoidal distribution, there is essentially no requirement on the shape of the initial laser pulse other than it be ultra-short (length τ_l much shorter than eventual beam length after space charge expansion). Thus such laser pulses are a natural, and technically achievable way of producing an ellipsoidal-shaped, nearly uniform density beam.

As the beam dynamics just after photoemission are qualitatively different in the traditional emittance compensation scenario and in the Luiten-Serafini scheme, it is not immediately apparent that one may successfully combine the two. The UCLA-SPARC collaboration has recently shown[5] that this marriage is indeed possible; further, the combination emittance compensation and dynamic creation of the ellipsoidal shaped beam produces results that in many ways are superior to those obtained in state-of-the-art designs. As the bunches produced are shorter than in such standard cases, very high brightness beam creation was shown to be possible.

The basic idea behind the Luiten-Serafini scheme is simple: the beam profile expands and deforms longitudinally to produce, in the final state, a

uniformly filled ellipsoid of charge. In the process, phase space rearrangements occur which degrade the emittances — especially in the longitudinal dimension. In order to understand this process, to specify experimental requirements, and to identify experimental signatures associated with the process, we have analyzed the dynamics of space-charge-dominated beam expansion[5].

This analysis may be summarized in a few points:

First, the injected bunch surface charge density $\sigma_b = dQ_b/dA$ must not be too high, or image charge effects at the cathode distort the final pulse profile so that it is not ellipsoidal. This is quantified by the condition $\alpha \equiv 4\pi\sigma_b/E_0 << 1$.

Second, the beam must be much shorter than its eventual size in order to be able to ignore the details of the initial pulse profile, which is not a serious constraint. In practice 300 fs laser pulses (typical of the limitations of the SPARC photocathode drive laser after conversion to UV) excite roughly the same length electron bunch, which expands to around 4 psec in our example cases. The pulse length after expansion is estimated as $L_b \approx 2\pi\sigma_b m_e c^2/E_0^2$.

The current density that is achieved after expansion, is $J_z = eE_0^2/4\pi m_e c$, a constant dependent only on the applied electric field E_0. All beams become uniform in density. To achieve the desired *ellipsoidal* beam shape, one must choose the initial surface current density distribution correctly, which implies that $\sigma_b(r) = \left(3Q/2\pi a^2\right)\sqrt{1-\left(r/a\right)^2}$.

Several phenomena that do not occur in a standard geometry ($\sigma_b(r) = $ constant) are apparent from this analysis. In the Luiten-Serafini scheme, pulse length expansion is required, while in the standard scenario it is avoided. During this expansion, one has mixing of electrons between slices. This causes an initial fast increase of the longitudinal emittance, which is terminated by the transition of the space-charge field direction from mainly longitudinal to predominantly transverse as the beam accelerates. The "missing" region of transverse space-charge also differentiates this scenario — the geometry of the injected beam in the standard configuration has a length much longer than the radius, and transverse space-charge forces assert themselves nearly immediately, within a propagation length approximately equal to the beam radius.

While the analysis of the beam dynamics is useful, the central issue of joining this regime with emittance compensation must be explored with simulations. The initial simulations begun in Ref. 5 we have performed are in the context of the SPARC scenario, so that we may proceed directly to discussing the experimental tests of this new regime — now commonly known as the "blowout regime" — of the photoinjector there.

2. Blowout regime with emittance compensation: general study

We have performed initial UCLA PARMELA[6] simulations to explore the joining the Serafini-Luiten scheme with the optimized emittance compensation working point, of the SPARC injector at LNF. We assume that the gun (1.6 cell, 2856 MHz) and solenoid are the same, and run near to the standard conditions. Through trials, we have optimized the launch conditions of the beam. In order to have values of α which do not give excessive image charge effects, the beam charge is lowered and the beam radius is slightly enlarged. In the preliminary optimization, we launch a 0.33 nC beam with an initial longitudinal Gaussian distribution having σ_t =33 fs beam, and a radial Gaussian with σ_x =0.77 mm (cutoff at 1.8 σ). The gun is run with a peak on-axis gradient of 120 MV/m; the beam is launched at 33 degrees forward of crest. This is advanced in comparison to the nominal launch phase for a standard bunch, and serves to control the excessive beam energy-spread after the gun. The emittance compensation solenoid is run with peak field B_z= 2700 G, which is slightly below the standard scenario, as the beam has slightly lower energy exiting the gun. We note that the peak value of α in our case is 0.11, as opposed to 0.42 in the LCLS design.
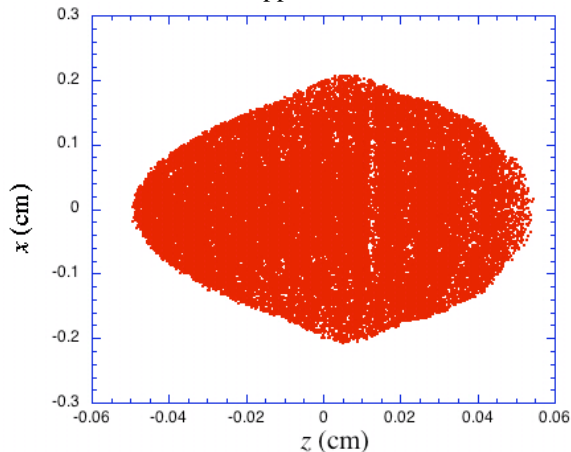

Figure 1. PARMELA simulation results, showing e- bunch (x, z) distribution 133 cm from cathode (6.3 MeV energy), before injection into first linac section, showing ellipsoidal beam boundary.

There is of course an initial transverse emittance growth which occurs during the reconfiguration of the bunch charge near the cathode, and subsequent growth which may occur due to the imperfections in the quasi-ellipsoidal distribution that is formed. It is these effects that are addressed by the emittance compensation process. Emittance compensation is accomplished in two steps: the focusing of the beam by the post-gun solenoid, and the matching of the beam in the first traveling wave linac section (3 m long, SLAC-type, 13.5 MV/m average acceleration), which has a 560 G solenoid field overlaid on it.

The formation of the quasi-ellipsoidal bunch is clearly shown in Fig. 1, which displays the bunch (x, z) distribution at a point 133 cm from the cathode, in the drift space after the gun and just preceding initial traveling wave linac section. Here the beam has 6.3 MeV mean energy, and its transverse dynamics are space charge-dominated. Thus one sees clearly the "inflated" ellipsoidal beam shape. As this shape is obtained purely through space-charge effects, the 6-dimensional transverse phase space is indeed close to the ideal Kapchinskii-Vladimirskii distribution. The final bunch length is 1.3 mm full width, corresponding to a peak current of 105 A. Thus even with one-third of the charge, this scheme should produce a higher current than obtained in simulations of the standard design.

Two notable defects are seen in the beam shape in Fig. 2. The first is the extension of the half-ellipsoid in the trailing part of the bunch as compared with the initial half. This asymmetry is caused by image-charge effects. This non-ideal behavior in fact gives the limit on α; when one attempts to launch a higher surface charge density, the bunch deformation from the desired symmetric ellipsoid produces poor emittance performance. The second notable feature is the existence of an anomalous ring at the outer radial edge of the beam. This part of the beam has low surface charge density and experiences radially fringing fields due to its edge location. Because of these effects, it does not experience enough longitudinal expansion to keep pace with the rest of the bunch, but instead has a moderate amount of radial expansion.
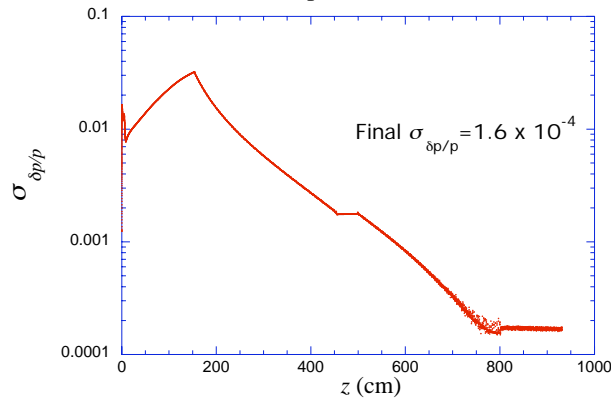
Figure 2. Evolution of $\sigma_{\delta p/p}$ in z for emittance compensation case, from PARMELA simulation.

As the longitudinal space charge during much of the acceleration is linear, and pulse length T is short, the longitudinal phase space is very compact. The evolution of the relative momentum spread $\sigma_{\delta p/p}$ in z is shown in Fig. 2. The final achieved rms value is $\sigma_{\delta p/p} = 1.6 \cdot 10^{-4}$, which is an order of magnitude smaller than that obtained in the standard LCLS-type (or SPARC-type) design.
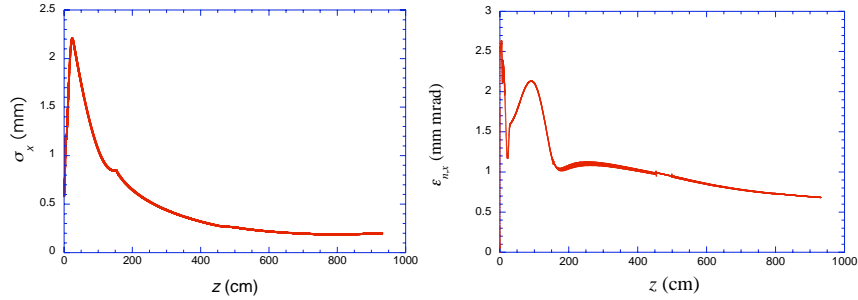
Figure 3. (left) The evolution of rms transverse beam size σ_x for emittance compensation case, fromPARMELA simulation. (right) Evolution of rms normalized emittance $\varepsilon_{n,x}$ for emittance compensation case.

The evolution of the rms transverse beam size σ_x, and the rms normalized emittance $\varepsilon_{n,x}$ are shown in Figs. 3. While the behavior of σ_x is similar in most respects to the standard design, with the beam approximately matched at linac entrance to the invariant envelope, the emittance behavior is not as familiar. In the standard LCLS design, $\varepsilon_{n,x}$ achieves a minimum value in the post-gun drift, rising to a local maximum at injection into the linac. The focusing and adiabatic damping of the motion in the linac then produce a monotonic decrease of $\varepsilon_{n,x}$ in z. In our case, the transverse space-charge and thus the plasma/emittance oscillations do not "turn on" until after the longitudinal expansion is well underway, thus delaying the emittance minimum in Fig. 3 to occur inside of the linac. In order to produce faster emittance oscillations in the linac to strongly diminish $\varepsilon_{n,x}$ before acceleration removes the plasma-dominated beam behavior, the solenoid field in the first linac section has been raised by 40% relative to the standard scenario. This ploy works well, as the final value (still slightly decreasing) of $\varepsilon_{n,x}$ at the end of the second linac (84.5 MeV energy) is 0.68 mm mrad. The thermal emittance at the cathode is 0.4 mm mrad, and so the space-charge induced emittance is well compensated.

After acceleration to higher energy (84.5 MeV), the beam is not space-charge dominated, and the (x,z) profile no longer ellipsoidal, as shown in Fig. 4. Nonetheless, the beam has excellent emittance, and maintains a current profile with shape $I(t) \propto \sqrt{1 - (2t/T)^2}$. With a high initial current, and low intrinsic energy spread, this beam may be compressed further, with very high final peak current achievable. In Fig. 5, we show the resulting longitudinal phase space calculated by a further simulation, using Elegant[7] (with input obtained from PARMELA output), of post-acceleration running forward of crest, and then encountering a chicane. The distribution shown has a final rms bunch length $\sigma_z = 11$ μm ($\sigma_t = 37$ fsec), with a peak current of 4.5 kA. This beam, which has

only 0.4% rms momentum spread, has obvious utility in ultra-short pulse FEL or inverse-Compton scattering experiments at SPARC.
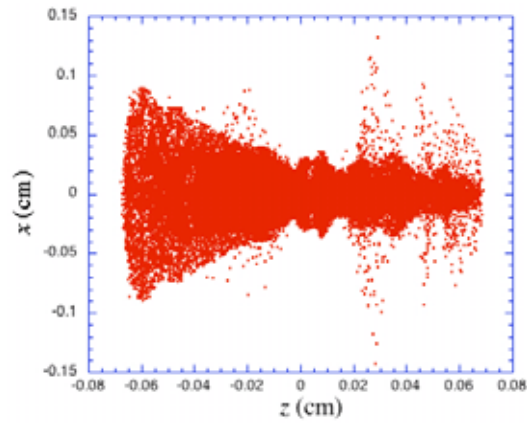
Figure 4. Electron bunch (x, z) distribution after second linac section (84.5 MeV energy), with ellipsoidal beam shape no longer apparent, from PARMELA simulation.
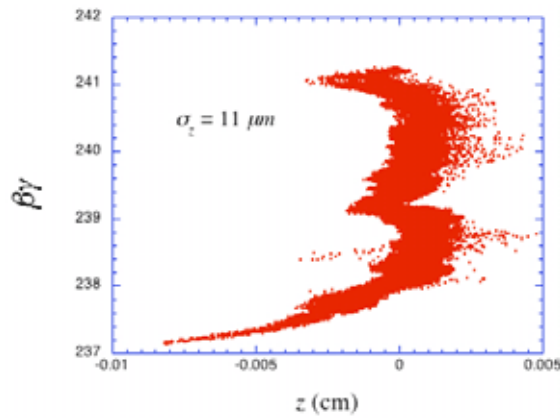
Figure 5. Longitudinal phase space after third (off-crest) linac section and chicane, showing compression of pulse to $\sigma_z = 11$ μm, from Elegant/PARMELA simulation.

3. Considerations for SPARC experiment

Several experimental scenarios have been investigated for possible tests of this new "blowout" regime of photoinjector operation, all at UCLA collaborating institutions. These laboratories include the PLEIADES injector, the ORION injector, and the SPARC injector. All have approximately the same

gun design (fabricated at UCLA), and have traveling wave post acceleration linacs with solenoid focusing overlaid. All of these injectors possess lasers with ~100 fs pulse capability, and are adequate for studying the physics of this regime. The PLEIADES injector has been placed on hiatus. The ORION injector is a bit different than what we have shown above, in that it employs X-band linac sections; this is a notable but not serious difference, and thus one may consider its use. Finally, we note that the SPARC injector is the example we have employed here, and is thus apparently nearly optimum for exploring the physics illustrated in the preliminary simulations above.

3.1. *Laser and photocathode issues*

Before discussing the planned electron beam measurements, we first review some experimental considerations specific to the use of such short lasers. First, we note that it should be tailored, either by collimating and relay imaging ("cut-Gaussian", as in the simulations); even better, more sophisticated manipulations of the laser intensity may be accomplished by use of a deformable mirror[8]. Provisions need to be made for having a high resolution "virtual cathode" to monitor the laser intensity profile at the cathode.

The beam must also be fairly short. In first measurements at SPARC, we have found, through cross-correlation measurements, that the UV pulse is difficult to make shorter than 300 fs using 3rd harmonic generation with noncollinear mixing in the conversion crystals. In order to obtain even this result, we must give up UV energy, going from 1.5 mJ to 0.2 mJ. While this energy is still adequate for obtaining 0.33 nC of charge using a metal cathode (Cu or Mg), to go shorter may be difficult. In order to check the effect of this extra pulse length on the scheme, we have performed simulations analogous to the original exploratory calculation. Indications are that the added length in the laser pulse does not affect the final electron beam configuration at this level.

The laser transport in this case is also complicated by illumination at 70 degrees. The needed time-transverse correlation on the laser pulse is introduced by a blazed grating. This procedure should be accurately implemented for this experiment in particular, as small time errors may be important. Also, it should be noted that the grating is a dispersive element, and the effect of having a large laser bandwidth should also be examined.

The laser intensity needed for this scenario is a factor of 30-100 higher than in the LCLS case. The issue of laser damage at both the input window and the cathode surface has been examined, and found based on previous experience at UCLA and at the BNL ATF to not be worrisome. A large laser field at the cathode can also produce a previously unanticipated effect, that of "heating" the electrons through the induced wiggling motion. The degree to which the laser field causes emittance growth can be estimated as

$$\varepsilon_n \cong a_l \sigma_x \cong \frac{\lambda_l}{2\pi m_e c^2} \sqrt{Z_0 P_l} \,.$$

(1)

Here a_l is the peak normalized vector potential of the laser field, and P_l is the peak laser power (note the independence of the beam size σ_x). For the SPARC experiment we estimate that $\varepsilon_n \approx 0.04 \, \text{mm-mrad}$, so this effect, while physically interesting, is negligible in our case.

One must also examine the issue of cathode time response. For a metal such as Cu, the laser penetrates only a conduction electron plasma skin-depth $l_d \cong k_p^{-1} \cong \left[4\pi r_e n_e \right]^{-1/2} \approx 50 \, \text{nm}$. An excited photoelectron born in this thin region must leave essentially normal to the surface, and travels with velocity $v \cong c \left[2h\nu_l / m_e c^2 \right]^{1/2} \approx 4.2 \cdot 10^{-3} c$. The time constant associated with the escape of the photoelectrons is thus $\tau_e \cong l_d / v_e \approx 40 \, \text{fs}$, so we should not have significant lengthening in this experiment. On the other hand, L-band photoinjectors with lower gradients (e.g. TTF) typically use Cs_2Te high quantum efficiency ($QE > 1\%$) cathodes. The higher QE arises from the scattering of the photoelectrons off phonons in the semiconducting material, and thus the emission process may be one to two orders of magnitude longer. This must be kept in mind before considering extending this scheme to an L-band scenario.

3.2. *Experimental signatures and measurements*

The experimental signatures that one looks for in tests of this photoinjector operating regime may be delineated. In general terms, the complete compensation scheme presented will show good emittance performance, along with a higher current and shorter pulses. In addition, at low energy, the beam will have an ellipsoidal shape. This shape may be viewed trivially in z-projection by a standard profile monitor (scintillating crystal, optical transition radiator, etc.). In terms of the longitudinal profile, one may consider use of a streak camera, to observe the time dependence of the current, and spatially resolve the transverse direction, thus measuring for example, a (x,z) slice of the beam, which should give a uniformly filled ellipse. By scanning this slice in x position, one may reconstruct the entire ellipsoid. Streak cameras may have time resolution as low as 0.25 ps (in practice it may be a bit larger), which is adequate to resolve the beam in our example, which is longer than 4 ps full width. The z-projected transverse phase space (in one dimension) may be investigated at low energy using the multi-slit technique.

At higher energy, one may observe the final state of well-compensated emittance through quadrupole scanning[9] or transverse phase space tomography[10]. The ellipsoidal beam is not observable at this energy, as the beam transverse distribution is emittance, and not space-charge dominated, as shown

in Fig. 4. The longitudinal distribution can be time-resolved at higher energy at the SPARC injector[11] using a fast RF sweeper with 30 fs resolution. One may also use longitudinal phase space tomography to observe the higher quality longitudinal phase space. In addition, at SPARC one may use a downstream compressor to investigate compression to the ultra-short bunch length illustrated in Fig. 5. This bunch length presents challenges in measurement, stressing both coherent radiation techniques, and RF deflectors.

In the SPARC experiment, we plan first to image the beam (time-integrated) at low energy (5-7 MeV) in the region after the gun, using a YAG detector. For time resolved measurements we will first convert the beam spatial information to photons with a prompt emitter. As transition radiation gives too weak of a signal at this energy, we will use a Cerenkov convertor (shown in Fig. 6). In order to have a manageably small-angle of emission we use aerogel, which has small index (n=1.005-1.02). At 5 MeV the Cerenkov emission threshold is reached for n=1.005; we may choose angles of emission from near zero at this threshold up to 9 degrees with the aerogels that are presently in-hand. The aerogels have been custom fabricated at the Jet Propulson Laboratory, using as a guide the mass/index relation $n = 1 + 2.1 \times 10^{-4} \cdot \rho\left(\mathrm{mg/cm}^3\right)$.


Figure 6. Cerenkov converter vacuum-tight holder, for containment of aerogel, with upstream entrance foil and downstream quartz window.

We presently are following the protocol of protecting the SPARC vacuum from out-gassing by the aerogel, developing an aerogel container as shown in Fig. 6. We have also studied the optical and vacuum properties of aerogel in order to optimize and simplify the design. The optical properties examined include the verification of the optical index and degree of scattering using green laser light (Fig. 7). These tests determined that the indices were as expected, and the scattering angles associated with green light were within the spreads already present due to Cerenkov and (scattered) beam angles.

At the same time, a program has been developed at UCLA to calculate, using a Monte Carlo approach the imaging and temporal resolution properties of the Cerenkov light from creation through transport to a final detector. As Cerenkov light has large angular spread (also enhanced by the entrance foil, with between 1 and 5 additional degrees of divergence from multiple scattering),

and broad wavelength spectrum, these properties must be examined carefully to ensure that the measurement will give the desired results.
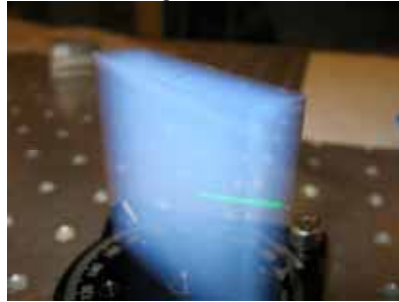
Figure 7. Testing of aerogel at UCLA, laser refraction determination of optical index.

The first step of the simulation is to provide electrons (typically 40,000) from PARMELA to GEANT, which simulates the scattering of the electrons in the entrance foil and generates a collection of Cerenkov photons in the aerogel. Optical transition radiation from the foil (weak) and very wide angle Cerenkov light generated in the output window (uncollected) are neglected in this simulation. The simulated distributions are filtered in wavelength — in practice this is accomplished with bandpass filtering in the downstream transport — and terminated at the output window. The photon distributions that result are then passed to a Mathematica-based, optical ray-tracing program, Rayica. Examples of these distributions are shown in Figs. 8 and 9.
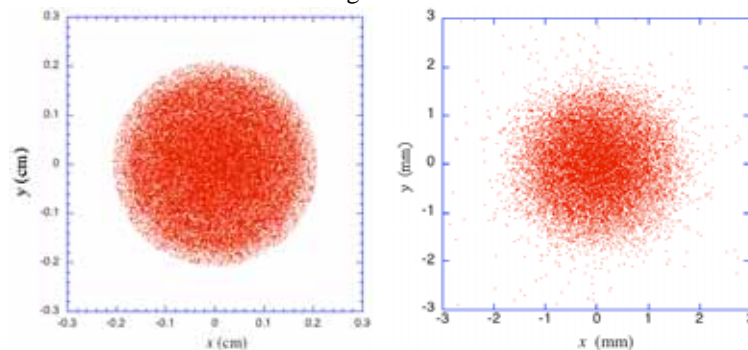
Figure 8. (Left) Electron beam distribution at aerogel holder input, from PARMELA; (right) photon distribution from GEANT at aerogel exit.

The GEANT simulations served to benchmark the analytical approximation to the number of photons obtained within a certain bandwidth $\Delta\omega/\omega$, that is $N_\gamma/N_{e^-} \simeq \alpha(2\pi/\lambda)\left[1-(\beta n)^{-2}\right](\Delta\omega/\omega)$, where α is the fine-structure constant. In Fig. 8, the transverse (x-y) distributions of electrons from PARMELA at the aerogel holder entrance and the analogous distribution of band-passed Cerenkov

photons from GEANT are given. It is seen that the electron beam distribution is smeared by the "depth-of-field" of the photons, emitted at large angles, and at depths in the aerogel as large as 3.5 mm. To illustrate the full effect of this smearing on a time-resolved, transverse imaging measurement of the beam, we show in Fig. 9 the *t-r* distribution of photons at the aerogel exit. A clear degradation of the nearly ellipsoidal beam boundary that was displayed in the electron beam distribution is seen in the photon distribution.
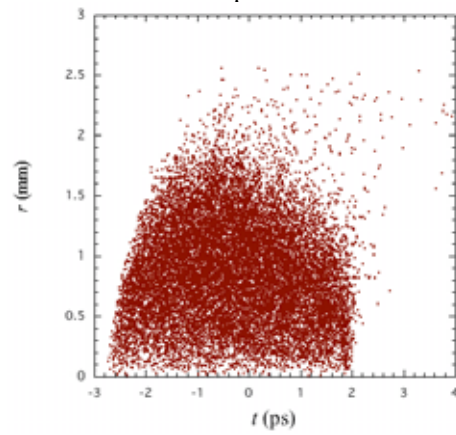
Figure 9. Photon distribution in radial position vs. time, from GEANT at aerogel exit.

In order to anticipate the quality of a time-resolved, transverse imaging measurement obtained with such Cerenkov photons, their transport to a detector has been simulated using Rayica. The transport system consists of an objective and focusing lens, with a field lens placed at the intermediate focal point located in between these lenses. The field lens serves to surpress "vignetting" of the imaged photons due to the simultaneous presence of large angles and a large initial field of Cerenkov photons.
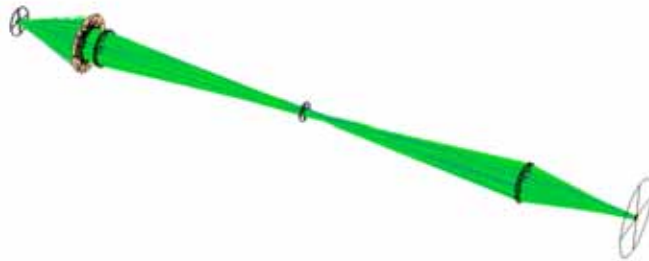
Figure 10. Optical transport line, with 10 % bandpass filter centered on 500 nm. Aerogel index of refraction n = 1.018.

Two examples of Rayica simulations are displayed in Figs. 10 and 11. In Fig. 10, we show the initially considered scenario, concentrating on the visible (500 nm) spectrum, with a relatively large index (n=1.018) and 10% bandwidth. This case was chosen in order to have a large photon yield, but had two unfortunate attributes: the photons have such a large angle that they are collimated by the output window (as seen in Fig. 10), and the temporal dispersion is unacceptable large. The first effect is mitigated by obtaining smaller n aerogel, which has been enabled by JPL. Smaller n also ameliorates the second issue, which is further improved by working at longer wavelength. Such a case is shown in Fig. 11, which displays a simulation considering 800 nm central wavelength ($\Delta\omega/\omega$=5%), and n=1.0084. The results of a series of simulations at this preferred central wavelength is given in Table 1.


Figure 11. Optical transport line, with 5 % bandpass filter centered on 800 nm. Aerogel index of refraction n = 1.0084.

Table 1. Summary of results obtained from GEANT-Rayica Cerenkov creation and transport simulations, 40,000 electrons, 5% bandwidth centered on 800 nm.

Index of refraction	Number of photons	Surviving fraction at detector
1.00525	528	92.23 %
1.0063	1109	89.54 %
1.00735	1674	86.49 %
1.0084	2259	84.10 %

It should also be noted that recent tests of aerogel performance during vacuum pump-down at UCLA have indicated that quite good vacuum levels (few 10^{-8} Torr) are achievable at the pump nearest near the aerogel. Further, the aerogel is undamaged when pump-down proceeds slowly. The excellent pumping characteristics of aerogel, which has all voids simply connected, are well known from its use in space exploration missions. We can therefore consider, subject to further testing, the elimination of both the upstream foil and the downstream window. This would serve to clean up multiple scattering and spurious OTR and Cerenkov production from the initial photon distribution.

At SPARC there is a streak camera that is being reconditioned to have 2 ps FWHM time resolution, which is on the border of resolving for the bunch length of interest. This is handled in initial measurements by use of higher charges (above 1 nC), and thus longer beams, to test the longitudinal expansion dynamics of the beam.
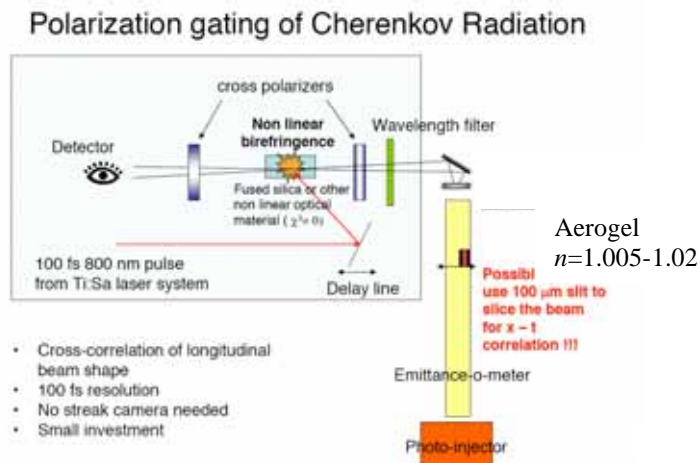
Figure 12. Schematic of multi-shot scanning, 100 fs resolution system based on polarization gating of nonlinear crystal. Horizontal collimation using slits allows scanning of transverse profile.

We must also consider alternative schemes based on ultra-fast gating. One such idea arising out of the SPARC program is summarized in Fig. 12, in which the Cerenkov light, appropriately limited in bandwidth, is injected into cross-polarizers, which nominally extinguish the light. Use of a crystal with nonlinear birefringence allows partial passage of the Cerenkov light when it is coincident with a strong gating laser pulse. This pulse will be derived from the 100 fs, 800 nm photocathode drive laser before frequency tripling.

It is instructive to review the polarization gating cross-correlation method in detail. The probe pulse is sent through crossed polarizers and a gate pulse is prepared with a polarization that is oriented at 45 degrees with respect to that of the probe pulse. The two pulses are then spatially overlapped in a piece of fused silica. In the fused silica, the gate pulse induces a birefringence through the electronic Kerr effect, a third-order optical nonlinearity, also known as the nonlinear refractive index. As a result, the fused silica acts as a wave plate while the gate pulse is present, rotating the probe pulse's polarization slightly, which allows some light to be transmitted through the analyzer. Because birefringence only occurs when the gate pulse is present, this geometry yields a cross-correlation of the probe pulse, if one measures the light energy transmitted through the analyzer as a function of optical delay between the two pulses.
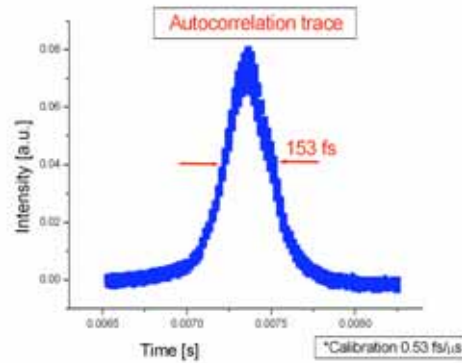
Figure 13. Example of autocorrelation of 100 fs IR beam in SPARC photoinjector laser system.

The amount of light transmitted depends on the intensity of the gate pulse following the relation $T = \sin\left(2.34\,\pi n_2 I\left(L/\lambda\right)\right)$, where L is the length of the nonlinear material, n_2 is the nonlinear index of refraction, λ is the central wave-length of the filtered Cerenkov radiation and I is the intensity of the gate pulse. The appropriate level of energy in the gate pulse is easily obtained in the SPARC case by focusing a portion of the infrared beam that is the residual of the harmonic conversion. Further, we note that the harmonic conversion is done at short pulse length in this experiment. Such beam is very short and intense (> 20 mJ) and there are problems is transporting it to the interaction region g, as well as in converting the IR to UV without too much pulse lengthening.

The initial laser pulse length must be monitored in the experiment, both in IR — to know the resolution of the gating measurement — and in the UV, to obtain the initial conditions of the photoelectron beam at the cathode. In order to illustrate the technique of autocorrelation needed to measure laser pulse lengths of pulses obtained already in the SPARC laser system, we show in Fig. 13 an autocorrelation of the laser in the IR. This test gave an autocorrelation of 150 fs, which corresponds to a pulse length (FWHM) of 100 fs.

As it is envisioned, the gating measurement is based on scanning with a delay line, and is thus a multi-shot (~100) technique. If we further desire to scan the transverse distribution by collimating the electron beam with a slit, the number of data points to construct one (x,t) profile is quite large. Thus, even though the polarization gating scheme is inexpensive and promises good resolution, thought must still be given to a single-shot measurement. At SPARC, a single shot measurement, based on the RF deflector, will be available only at high energy, where the ellipsoidal beam is not observable. The 10 fs resolution of this time measurement should provide details of the dynamics not available through other methods, however.

3.3. *Recent simulation work*

The preliminary UCLA PARMELA simulations discussed above closely approximate the SPARC scenario, but do not provide an exact model yet for the experiments we propose. To this end, further simulations using UCLA PARMELA, Los Alamos PARMELA (at INFN-LNF), and TREDI (at ENEA) are being performed at present. We show the results of new simulations of the reference design from UCLA PARMELA in Figs. 14 and 15. The first major difference introduced is the assumed lengthening of the injected beam, due to harmonic crystal and cathode response times, to 310 fs FWHM (4 times the case simulated above). As can be seen in Fig. 14, the overall ellipsoidal shape (shown at z=133 cm) is not notably changed from that shown in Fig. 1. The emittance compensation performance (Fig. 15) is acceptable, if a bit less effective than in the shorter launch beam case. We note however, that the working point has not been reoptimized in this case, as linac and solenoid settings have not been readjusted. Further optimization studies are being done to understand the baseline design for the experiment, as well as tuning/jitter performance curves for *e.g.* solenoid strength, linac phases, injection jitter, etc.
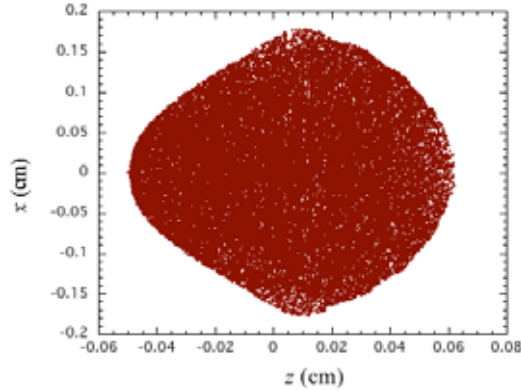

Figure 14. PARMELA simulation results, showing electron bunch (x, z) distribution 133 cm from cathode for case with 310 fs FWHM pulse length, taking into account possible lengthening mechanisms in harmonic crystal and cathode response.

Simulations studies have examined pulse compression in the SPARC chicane (with PARMELA, and Elegant). The success of these studies are represented by the longitudinal phase space post-compression shown in Fig. 16. It can be seen that the quite linear longitudinal phase space pre-compression allows an extremely short beam (11 μm rms) to be produced by compression.

Further computational investigations planned include examination of velocity bunching using PARMELA; TREDI will also be used to model the effects of cathode emission nonuniformities and other 3D phenomena. It is also

of crucial importance to evaluate the performance of a SASE FEL driven by dynamically optimized beams at SPARC.
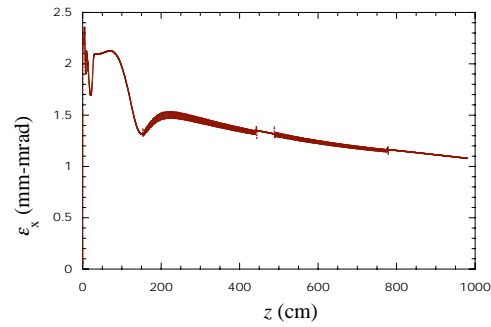
**Figure 15**. Emittance evolution for case shown in Fig. 14.
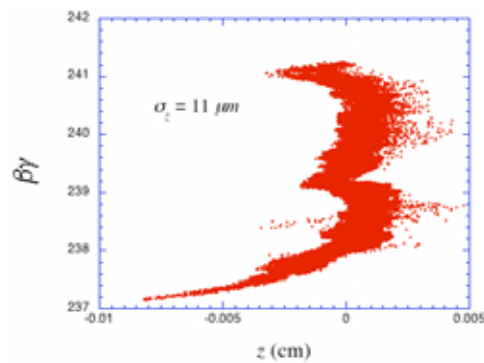
Figure 15. Simulated longitudinal phase space at SPARC, post-compression, from PARMELA.

4. First results

The first stage of experimentation on the blowout regime took place at LNF beginning at the end of March, 2006. These took place in the context of the commissioning of the RF photocathode gun alone. Upon startup, the UCLA-produced gun was conditioned quickly up to 11 MW, which produces 110 MV/m peak electric field, and 5.7 MeV electron beam. Here we describe preliminary measurements made with this system

With the laser reconfigured for short pulse (less than 0.5 psec FWHM), up to 1.6 nC of charge. While the laser was set to approximately the correct transverse size and profile shape, there remained considerable spatial fluctuations in both the laser and cathode quantum efficiency. Thus the conditions for observing the dynamic creation of nearly uniformly filled ellipsoidal charge distributions were not quite present; in fact, the emittance was

not of equivalent quality to that obtained in standard operation. Nevertheless, impressive first data were obtained.
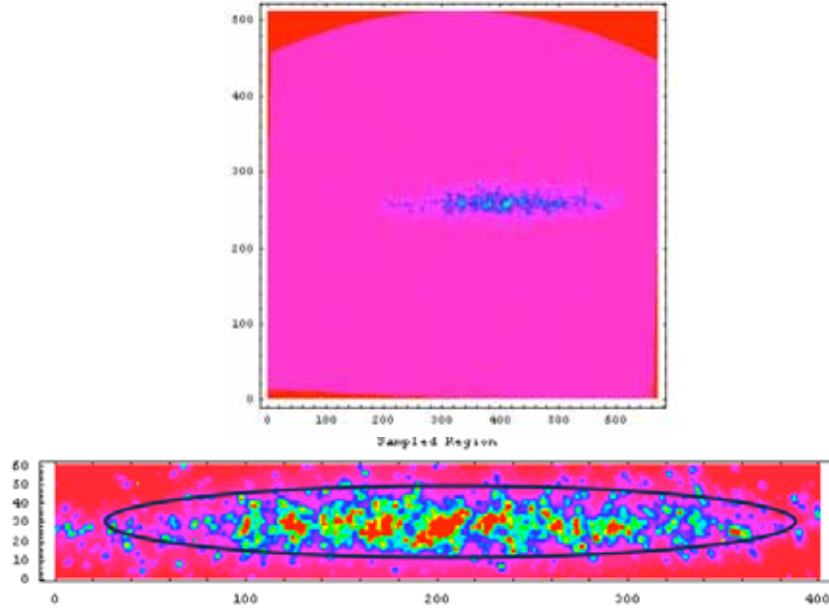
Figure 16. (top) Streak image after image correction from SPARC experiment, 150 psec total window in vertical dimension; (bottom) area of interest in streak image, with elliptical contour shown for analysis purposes.

Initial measurements of the beam's longitudinal-transverse profile were made with aerogel with index n=1.008, with the Cerenkov radiator placed 2.4 m away from the cathode, downstream of the slit-based emittance measurement system. Streak camera images were obtained using the transport system described in the previous section. A complication arose from the correction applied to the streak image which corrects for the aberrations in the streak tube itself. A time-transverse correlation was introduced by this correction scheme which then had to be removed in analysis. Such a streak, after correction, is shown in Figure 16. This image displays the profile obtained from a bunch with charge of 700 pC. A large charge is preferred in this case in order to discern information at a time scale longer over the streak camera resolution; the 700 pC case is expected to have expansion of approximately 7 psec FWHM, well in excess of this 2 psec FHWM resolution.

Streak images obtained in the highest temporal resolution mode are inherently noisy; this condition is required in order to avoid space-charge induced pulse distortion inside of the streak tube. Thus in order to extract information from single shots concerning the streak image — which should

represent the beam density distribution in an *x-z* slice in the midplane of the bunch — we have adopted a maximum likelihood analysis to test for different assumed types of beam distributions.

The *x-z* slice distributions we have tested for consistency with the data include: (1) a bi-Gaussian (thermal-type) distribution; (2) a uniformly filled ellipse (assumed arising from a parent uniformly filled ellipsoid); and (3) a nearly uniformly filled ellipse with a tail, which we choose to represent as a Fermi-Dirac distribution.

As all of the distributions assumed have contours of constant density that are elliptical, a systematic statistical approach is possible, in which we look at the total integrated intensity inside of ellipses of size varying from zero area to an area covering the entire streak image. These ellipses, an example of which is shown in Fig. 16, are all required to have the same aspect ratio, which is given by the intensity profile itself, $R = \sigma_x / v_s \sigma_t$ (v_s is the streak velocity, and σ_t = 3.45 psec for the streak in Fig. 16).
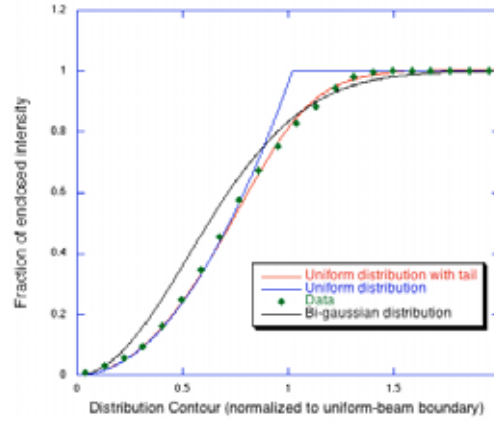
Figure 17. Analysis of streak data, with fraction of integrated intensity of data inside of elliptical contour shown. Best fit of data points to three models are shown: bi-gaussian distribution, uniform elliptical distribution, and Fermi-Dirac (uniform with tails) distribution.

The bi-Gaussian distribution is given by

$$f(x,t) = f_0 \exp\left[-\frac{1}{2}\left(\left(\frac{x}{\sigma_x}\right)^2 + \left(\frac{v_s t}{v_s \sigma_t}\right)^2\right)\right] = f_0 \exp\left[-\frac{1}{2}A^2\right], \qquad (2)$$

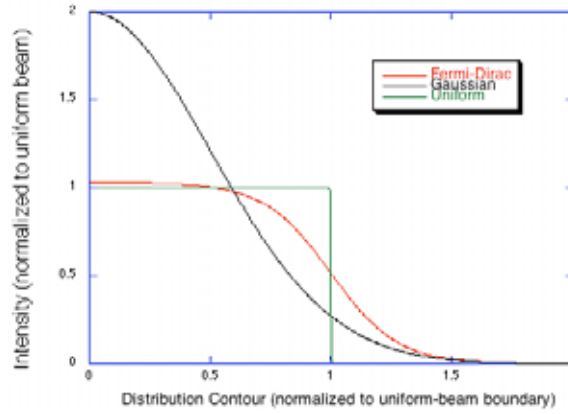with normalized integrated signal inside of the contour of amplitude *A*

$$I_1(A) = 1 - \exp\left[-\frac{1}{2}A^2\right]. \qquad (3)$$

Likewise, for a uniformly filled ellipse, one finds that the integrated signal inside of a contour of amplitude *A* is

$$I_2(A) = \begin{cases} A^2, & A \leq 1 \\ 1, & A > 1 \end{cases}. \tag{4}$$

Finally, for a Fermi-Dirac function in which the density profile is assumed to have amplitude dependence $\left[\exp\left(\alpha(A - A_0)\right) + 1\right]^{-1}$, the integrated signal inside of a contour of amplitude A is

$$I_3(A) = A^2 - \frac{2}{\alpha^2}\ln\left[\frac{1 + \exp\left(\alpha(A - A_0)\right)}{1 + \exp\left(-\alpha A_0\right)}\right] - \frac{2}{\alpha^2}\left[\text{Poly}\log\left[2, -\frac{\exp\left(\alpha(A - A_0)\right)}{\exp\left(-\alpha A_0\right)}\right]\right]. \tag{5}$$

Figure 18. Analysis of streak data, with fraction of integrated intensity of data inside of elliptical contour shown. Best fit of data points to three models are shown: bi-gaussian distribution, uniform elliptical distribution, and Fermi-Dirac (uniform with tails) distribution.

With these functions in hand, we can fit to the data given in the streak images to determine the likelihood that one of the assumed three profiles is more likely than the others. Such an exercise has been performed for the streak given in Fig. 16, with the results shown in Fig. 17. It can be seen the bi-Gaussian hypothesis can be rejected as the least likely model. While the uniformly filled ellipsoid gives a good fit near the distribution center, it is not very accurate at the edge, where one expects strong deviations in any case from this model. Finally, we note that the best fit obtained from the Fermi-Dirac model (using α and A as fit parameters), gives an excellent match to the data.

The reconstruction of the distributions deduced from likelihood fits to the data in Fig. 17 are displayed in Fig. 18. It can be seen that the bi-Gaussian distribution is in large disagreement with the other two models, as it must be more peaked in the center — nearly a factor of two denser in our case. Note that the best fit, that of the Fermi-Dirac distribution, has a fall-off which can be attributed mainly to the approximately 2 psec full width half-maximum resolution of the streak camera, and thus expected physical erosion of the beam

edges, as well as artifacts from the initial sub-psec beam pulse profiled are hidden in this measurement.

5. Conclusions

While the first measurements have established the soundness of the basic experimental approach, and given tantalizing first evidence for the formation of a nearly uniform ellipsoidal distribution, much more remains to be done. In order to more tightly control the initial conditions, it is necessary to correct the emission profile from the cathode. As of now, the SPARC injector is being modified to allow for near-axis, as opposed to 70 degree, injection. Additional improvements should result from use of laser cleaning of the cathode, as well a deformable mirror, thus making the emitted charge distribution more in line with expectation. In this scenario, we also expect improvement of the emittance obtained, to yield levels at or below those of the standard operating scenario.

After the next round of experiments, the SPARC injector will be completed with the addition of post-acceleration linacs and beam diagnostics (*e.g.* RF sweeper). In this fully mature experimental scheme, a complete test of the consistency of the Luiten-Serafini scheme with emittance compensation should be possible, using the large array of techniques described here. Further experiments will also emphasize the demonstration of high quality longitudinal phase space, and concomitant low energy spread as well as high compressibility.

Acknowledgments

References

1. Luca Serafini and J.B. Rosenzweig Physical Review E 55, 7565 (1997).
2. I.M. Kapchinskii and V.V. Vladimirskii, in Proceedings of the International Conference on High Energy Accelerators, CERN, Geneva (Scientific Information Service CERN, Geneva, 1959), p. 274.
3. L. Serafini, AIP Conf. Proc. 413, 321 (1997).
4. O. J. Luiten, S. B. van der Geer, M. J. de Loos, F. B. Kiewiet, M. J. van der Wiel, Phys. Rev. Lett., 93, 094802-1 (2004).
5. "Emittance compensation with dynamically optimized photoelectron beam profiles" J. B. Rosenzweig, A.M Cook, R.J. England, M. Dunning, S.G. Anderson, Massimo Ferrario, Nucl. Instrum. Methods A, 57 87 (2006)
6. E. Colby, UCLA PhD Thesis, FERMILAB-THESIS-1997-03 (FNAL, 1997)
7. M. Borland, computer code ELEGANT, ANL, http://www.aps.anl.gov/asd/oag/oaghome.shtml.
8. http://www.okotech.com
9. X. Qiu et al., *Phys. Rev. Lett.* **76**, 3723 (1996).
10. V.Yakimenko, et al Phys. Rev. ST Accel Beams, 122801 (2003).
11. J.B. Rosenzweig *et al.*, "RF and Magnetic Measurements on the SPARC Photoinjector and Solenoid at UCLA", in Proc. 2005 Part. Accel. Conf. (IEEE, 2005).